

# Global warming and ocean stratification: a potential result of large extraterrestrial impacts

Manoj Joshi<sup>1,2</sup>, Roland von Glasow<sup>1</sup>, Robin S. Smith<sup>3</sup>, Charles G. M. Paxton<sup>4</sup>, Amanda C. Maycock<sup>5</sup>, Daniel J. Lunt<sup>6</sup>, Claire Loptson<sup>6</sup>, Paul Markwick<sup>7</sup>

<sup>1</sup> Climatic Research Unit, School of Environmental Sciences, University of East Anglia, Norwich, U.K.

<sup>2</sup> Centre for Ocean and Atmospheric Sciences, School of Environmental Sciences, University of East Anglia, Norwich, U.K.

<sup>3</sup> National Centre for Atmospheric Science, University of Reading, U.K.

<sup>4</sup> Centre for Research into Ecological and Environmental Modelling, University of St Andrews, St Andrews, U.K.

<sup>5</sup> School of Earth and Environment, University of Leeds, Leeds, U.K.

<sup>6</sup> School of Geographical Sciences, University of Bristol, Bristol, U.K.

<sup>7</sup> Getech PLC, Leeds, U.K.

Corresponding author: Manoj Joshi

## Key Points:

- Large increases in stratospheric water vapor following large bolide impact events over the ocean cause positive radiative forcings
- Impact events are capable of warming climate and stratifying upper ocean over 1-2 decades even after initial surface cooling
- The process could have significantly reduced or possibly even reversed decadal cooling following Chicxulub impact

## 37 Abstract

38 The prevailing paradigm for the climatic effects of large asteroid or comet impacts is a reduction  
39 in sunlight and significant short-term cooling caused by atmospheric aerosol loading. Here we  
40 show, using global climate model experiments, that the large increases in stratospheric water  
41 vapor that can occur upon impact with the ocean, cause radiative forcings of over  $+20 \text{ Wm}^{-2}$  in  
42 the case of 10-km sized bolides. The result of such a positive forcing is rapid climatic warming,  
43 increased upper-ocean stratification and potentially disruption of upper-ocean ecosystems. Since  
44 two thirds of the world's surface is ocean, we suggest that some bolide impacts may actually  
45 warm climate overall. For impacts producing both stratospheric water vapor and aerosol loading,  
46 radiative forcing by water vapor can reduce or even cancel out aerosol-induced cooling,  
47 potentially causing 1-2 decades of increased temperatures in both the upper ocean and on the  
48 land surface. Such a response, which depends on the ratio of aerosol to water vapor radiative  
49 forcing, is distinct from many previous scenarios for the climatic effects of large bolide impacts,  
50 which mostly account for cooling from aerosol loading. Finally, we discuss how water vapor  
51 forcing from bolide impacts may have contributed to two well known phenomena: extinction  
52 across the Cretaceous/Paleogene boundary, and the deglaciation of the Neoproterozoic snowball  
53 Earth.

## 54 1 Introduction

55 The effects of asteroid or comet impacts range from regional environmental devastation  
56 to potential contributions to mass extinctions [Toon *et al.*, 1997, Alvarez *et al.*, 2009, Schulte *et*  
57 *al.*, 2010]. It has usually been assumed that the climatic effect of a large impact over a few years  
58 is surface cooling, caused by large amounts of aerosols such as dust, soot and sulphate being  
59 lofted into the middle atmosphere, which lowers the amount of solar radiation reaching the  
60 surface [e.g. Covey *et al.*, 1994]. However, if an object impacts on the deep ocean, large amounts  
61 of water are released into the atmosphere [Toon *et al.*, 1997, Pierazzo *et al.*, 2010]; the resulting  
62 increase in stratospheric water vapor (henceforth SWV) can then act as an additional, significant  
63 radiative forcing agent.

64 Unlike aerosol, SWV does not sediment out of the stratosphere providing the  
65 environment remains sub-saturated, so its radiative effect on climate is likely to last longer than  
66 that of aerosol. Previous studies have concluded that approximately 10-300 parts per million  
67 (henceforth ppm), of SWV might remain in the stratosphere for several years following the  
68 impact of an extraterrestrial body, depending on its size [Emiliani *et al.*, 1981, Toon *et al.*, 1997,  
69 Pierazzo *et al.*, 2010]. Aerosol forcing is likely to be much smaller unless the bolide is large  
70 enough to strike the bottom of the ocean [Covey *et al.*, 1994, Toon *et al.*, 1997]. The climatic  
71 effects of such a combined aerosol and stratospheric water vapor scenario are therefore important  
72 to quantify due to the high likelihood of a bolide striking the ocean as opposed to land.

73 To date, 3-D modelling studies have only examined the climatic effects of bolides  
74 of size 0.5-1 km, but the Chicxulub impact event at the end of the Maastrichtian is thought to  
75 have been caused by a bolide of approximate size 10 km [e.g. Schulte *et al.*, 2010]. Furthermore,  
76 past modelling studies did not examine the response of the ocean or its circulation [Pierazzo *et*  
77 *al.*, 2010]. Quantification of the surface climatic response to SWV from impactors significantly  
78 larger than 1 km, having an order of magnitude more kinetic energy [Toon *et al.*, 1997], has been  
79 limited to inferences from idealized single-column models [Toon *et al.*, 1997].

80 Here, for the first time, we perform ensembles of 3-D coupled-ocean atmosphere model  
81 simulations and simplified energy-balance-type calculations to quantify multi-year effects of  
82 combined SWV and surface shortwave radiation perturbations resulting from hypothesized  
83 impact events larger than 1 km in size; we restrict our simulations to those regimes where the  
84 response is likely to be qualitatively different to cooling induced by virtual extinction of sunlight,  
85 noting that a very large reduction in surface shortwave radiation is inconsistent with evidence  
86 suggesting that photosynthesis and export productivity did not cease across the K-Pg bolide  
87 event [Alegret *et al.*, 2012], and certain organisms did not die out (see section 4), suggesting that  
88 low-latitude land regions did not completely freeze. Using the results from our semi-idealised  
89 modelling experiments, we discuss the potential application of our results to the Chicxulub  
90 impact event at the end of the Maastrichtian and their potential relevance in the context of  
91 deglaciation of the Neoproterozoic snowball Earth.

## 92 2 Methods

93 Two models are used in the analysis: FAMOUS ((FAst Met Office/UK Universities Simulator)-  
94 a coupled-ocean-atmosphere model, and a simpler energy balance model or EBM.

### 95 2.1 FAMOUS

96 FAMOUS is a coupled ocean-atmosphere global circulation model of horizontal  
97 resolution  $7.5^\circ \times 5^\circ$  (longitude x latitude) in the atmosphere and  $3.75^\circ \times 2.5^\circ$  in the ocean [Smith  
98 *et al.*, 2012a], and has been widely used in studies of climate and paleoclimate [e.g. Smith *et al.*,  
99 2012b]. FAMOUS has near-identical physics and dynamics to the HadCM3 version of the Met  
100 Office Unified Model (MetUM) [Gordon *et al.*, 2000], which was used in the latest IPCC report,  
101 but is run at a lower spatial resolution. FAMOUS has the advantage of being computationally  
102 efficient, enabling the very long simulations required to spin up the ocean circulation for  
103 Maastrichtian boundary conditions, while retaining the complexity of a coupled-ocean  
104 atmosphere model utilizing the primitive equations of motion. Since it is not computationally  
105 feasible to run a full stratosphere-resolving chemistry-climate model on these timescales, and  
106 because we are primarily interested in the radiative rather than dynamical effects of stratospheric  
107 perturbations on the troposphere and surface, we focus on validating the radiative forcings  
108 (henceforth RF) and climate sensitivity simulated by FAMOUS against more complex models.  
109 Land average and global average surface air temperatures are  $15.1 \pm 0.1^\circ\text{C}$  and  $23.0 \pm 0.1^\circ\text{C}$   
110 respectively in the “Maastrichtian” control run, and  $8.0 \pm 0.1^\circ\text{C}$  and  $14.8 \pm 0.1^\circ\text{C}$  in the  
111 “preindustrial” run- all of which are within  $2^\circ\text{C}$  of values obtained by other modelling work  
112 [Hunter *et al.*, 2013].

113 We apply the SWV RF by adding a globally constant water vapor perturbation to the  
114 atmosphere’s radiative properties only (i.e. as seen by the model’s radiation code) to all levels  
115 within the model’s stratosphere, in a similar manner to previous work with versions of the  
116 MetUM [Maycock *et al.*, 2013]. The assumed SWV perturbations are shown in Table 1 and are 3  
117 - 150 times ambient mixing ratios of 2-5 ppm, which is well within the range of SWV  
118 perturbations due to bolide impacts estimated in earlier studies [Toon *et al.*, 1997, Emiliani *et al.*,  
119 1981]. The RF in the P, M, MD cases in Table 1 have been calculated using the method of  
120 Gregory *et al.* [2004]. The 3-6 year decay timescale of the SWV perturbation is chosen to be  
121 consistent with observations of age of air in the stratosphere [Engel *et al.*, 2009], and is shown in

122 Fig. S1(a). Offline RF calculations using the Edwards and Slingo radiative transfer code  
123 [Maycock *et al.*, 2011] incorporating a higher resolution representation of the stratosphere reveal  
124 differences in RFs between FAMOUS and the full radiative code of less than 10% (see S1).  
125 Water vapor in the troposphere in FAMOUS is transported and evolves self-consistently with the  
126 surface and hydrological cycle.

127 The effects of aerosol RF associated with a large impactor hitting the ocean bottom and  
128 lofting rocky ejecta into the atmosphere is approximated in the FAMOUS simulations by a  
129 reduction in the top-of-atmosphere solar forcing by 30%, equivalent to a top-of-atmosphere RF  
130 of  $-102 \text{ Wm}^{-2}$ , which causes a surface shortwave RF whose maximum amplitude is  $-55 \text{ Wm}^{-2}$ .  
131 Larger values of solar dimming of up to  $-80 \text{ Wm}^{-2}$  are explored in the EBM. Aerosol  
132 sedimentation is parameterized by keeping the solar forcing perturbation constant for one year,  
133 followed by an exponential decrease in the perturbation over a timescale of one year, consistent  
134 with previous work [Pierazzo *et al.*, 2003], and is shown in Fig. S1(b). The maximum RF is  
135 lower than estimates from large impact events [Pierazzo *et al.*, 2003]. However, it should be  
136 noted that the RF value used in the present work is shortwave only: the forcing from aerosol  
137 particles greater than  $1 \mu\text{m}$  in size is a residual of positive longwave and negative shortwave  
138 forcings that can each be much larger [e.g. Timmreck *et al.* 2010]. Recent work has suggested a  
139 range of short wave radiative forcing from soot aerosol from the Chicxulub impact of  $-100$  to  $-$   
140  $200 \text{ Wm}^{-2}$  [Kaiho *et al.*, 2016], implying a total surface radiative forcing that was lower in  
141 magnitude than this. Again, we note that a very large reduction in surface shortwave radiation is  
142 inconsistent with evidence suggesting that photosynthesis and export productivity did not cease  
143 across the K-Pg event [Alegret *et al.*, 2012], and certain organisms did not die out (see section 4),  
144 suggesting that low-latitude land regions did not completely freeze.

145 Each of the FAMOUS perturbation experiments is made up of 3 ensemble members  
146 which are each 50 years long, initialized from different points of the control run separated by 10  
147 years in order to sample the effects of internal variability in the model. The model is run in two  
148 configurations: one representing the preindustrial Holocene Earth, and one representing the  
149 Maastrichtian stage 72.1-66.0 million years ago, in order to assess the sensitivity of our results to  
150 continental configuration (see Table 1). For more details of FAMOUS boundary conditions and  
151 configuration see Text S1.

## 152 2.2 Energy Balance Model (EBM)

153 The EBM resolves hemispheres and land-ocean contrasts, and represents heat exchange  
154 in the ocean using an upwelling-diffusion model [Shine *et al.*, 2005]. The EBM assumes an  
155 equilibrium climate sensitivity parameter  $\lambda = 1.0 \text{ K (Wm}^{-2})^{-1}$ , mixed layer depth = 75 m, and  
156 ocean diffusion  $\kappa = 7.5 \times 10^{-5} \text{ Km}^{-2}\text{s}^{-1}$ , so that the land and ocean temperature response in the  
157 absence of aerosol RF is similar to that of ensemble M3. The value of  $\lambda$  is consistent with the  
158 climate sensitivity of FAMOUS (see Text S1). The EBM is computationally very cheap and  
159 therefore ideal for investigating responses to many RF scenarios [Shine *et al.*, 2005, Appendix  
160 B]. Here, 336 EBM runs are performed with a combination of RF sources from SWV and solar  
161 dimming. The maximum SWV RF in the EBM is varied from  $+10$  to  $+25 \text{ Wm}^{-2}$ , corresponding  
162 to SWV perturbations of approximately 50 ppm to 300 ppm, and has the same time evolution as  
163 FAMOUS, shown in Fig. S1(a).

### 164 3 Results

165 We first examine the effects of SWV perturbations only (i.e. scenarios P1-P3 and M1-  
166 M3). A key measure of the environmental effects of any climatic forcing is the change in surface  
167 air temperature that it induces [Collins *et al.*, 2013]. Fig. 1 (a) shows area-averaged surface air  
168 temperature change over ocean (henceforth OSAT) and land (henceforth LSAT) in the two  
169 decades following the input of the SWV perturbations designed to mimic the possible effects of  
170 different sized bolide impacts into the deep ocean. The size of the response increases with SWV  
171 perturbation magnitude, with the largest perturbations of 300 ppm (in scenarios P3 and M3; see  
172 Table 1), exhibiting maximum OSAT increases of 5 K and 8 K respectively, and maximum  
173 LSAT increases of 9 K and 11 K respectively (see Fig. 1b), a few years after the impact.

174 The time at which the maximum temperature change occurs relative to the simulated  
175 impact increases in proportion with the temperature change, being 2-3 years for the smallest  
176 values (P1 and M1), to 5 years for the largest (P3 and M3). In general, LSAT changes show the  
177 same lag-time as OSAT changes, but are amplified by a factor of approximately 1.5. Without  
178 aerosol forcing, the rates of warming are more than an order of magnitude faster than the rate of  
179 global warming expected over the 21<sup>st</sup> century, and the warming patterns also display polar  
180 amplification (See Fig. S2), which is a well-known pattern of climatic change [Collins *et al.*,  
181 2013]. The differences between the responses for the present-day and Maastrichtian conditions is  
182 related to the albedo in each configuration. Run M0 has a lower planetary albedo than P0: 0.27  
183 compared to 0.31, mostly due to lack of sea-ice in the warmer southern polar regions, which  
184 explains the former's higher globally averaged surface temperature. In addition, the maximum  
185 reduction in albedo following the input of the SWV perturbation is 12% in M3 compared to 3%  
186 in P3, suggesting a much stronger positive shortwave feedback in the Maastrichtian  
187 configuration, in addition to a stronger water vapor feedback due to higher concentrations of  
188 water vapor in the warmer atmosphere.

189 A key aspect of the warming signal is that it is not confined to the surface, but penetrates  
190 quickly into the upper ocean, increasing the static stability of this region, and inhibiting vertical  
191 motion. Such a response can restrict the transport of nutrients to the uppermost layers of the  
192 ocean [Roemmich and McGowan, 1995, Oerder *et al.*, 2015], potentially disrupting surface  
193 oceanic ecosystems. Fig. 2 shows cross sections of the ocean temperature response averaged  
194 over years 1-10 after the SWV perturbation is imposed in a sample of the model ensembles: P2  
195 (Fig. 2a), P3 (Fig. 2b), and M3 (Fig. 2c). In the tropics and subtropics, the warming response is  
196 confined mostly to the upper 100m of ocean. In the northern midlatitudes and southern subpolar  
197 regions, the warming signal penetrates downwards to 200-300m in depth. The scenarios with the  
198 largest increase in SWV display increases in upper ocean stratification whose consequences are  
199 to lower the magnitude of upwelling by up to 50% in upwelling regions (see Fig. S3), which are  
200 the regions where the majority of primary productivity occurs (e.g. Gregg *et al.* 2003). Key to  
201 this stratification is the rapid timescale of the warming (see Fig. 1).

202 As noted above the Chicxulub impact, which is thought to have contributed to the  
203 Cretaceous–Palaeogene extinction event (henceforth K-Pg event), approximately 66 million  
204 years ago [Alvarez *et al.*, 1980, Schulte *et al.*, 2010], likely caused significant injections of  
205 aerosols into the stratosphere by striking the ocean bottom [Toon *et al.*, 1997, Covey *et al.*,  
206 2009]. We examine the combined effect of such a joint aerosol-SWV scenario in two ways:

207 firstly by introducing a parameterization of aerosol-induced surface cooling into the FAMOUS  
208 model (See Section 2.1); secondly by using the EBM, to quantify the sensitivity of OSAT and  
209 LSAT responses to uncertainties in SWV and surface shortwave radiative forcing.

210 LSAT and OSAT in the M2D and M3D “SWV plus solar dimming” FAMOUS  
211 experiments are shown by blue and red diamonds in Fig. 1 (a), and (b), respectively. Even with a  
212 change in surface shortwave radiation of  $-55 \text{ Wm}^{-2}$ , ensemble M3D still exhibits a warming of up  
213 to 4 K (red diamonds), over 1-2 decades due to the warming effects of the SWV perturbation.  
214 Again, associated with the rapid warming is increased stratification of the ocean (see Fig. 2 (d)),  
215 which is not as large as that induced by SWV forcing alone (ensemble M3; Fig. 2 (c)), but does  
216 still cause a significant reduction in ocean upwelling (Fig. S4).

217 The climatic effects of a much larger range of SWV and surface shortwave radiative  
218 perturbations can be illustrated using the EBM. Fig. 3 shows land and ocean temperature  
219 responses in EBM runs that combine different magnitudes of cooling due to reduced surface  
220 shortwave radiation and warming due to increased SWV, with forcings in the four Maastrichtian  
221 climate model ensembles added for comparison. For certain combinations of forcings (e.g. a  
222 maximum negative surface RF =  $-40 \text{ Wm}^{-2}$  and a maximum SWV RF =  $+24 \text{ Wm}^{-2}$ ) it is possible  
223 for the EBM to respond with a land temperature change that is negative (regions with cold  
224 colours in Fig. 3 (a)), even though the largest upper ocean temperature change is positive (warm  
225 colours in Fig. 3 (b)), which implies an initial cooling of the land due to reduced sunlight,  
226 followed by warming of both land and ocean on a timescale of a decade or more.

#### 227 4. Discussion and Conclusions

228 These results may shed new light on understanding changes in the environment and  
229 ecosystems around the K-Pg event. Terrestrial species are likely to have been adversely affected  
230 by immediate effects such as fires and a decrease in solar radiation [Toon *et al.*, 1997, Schulte *et*  
231 *al.*, 2010], and ocean productivity might be expected to be hindered by reduced sunlight in the  
232 first couple of years due to significant aerosol loading. However, accounting for the possible  
233 effects of SWV increases following a large impact to the ocean suggests possible longer term  
234 warming over land and enhanced ocean stratification, which may have adversely affected many  
235 oceanic and terrestrial species for at least a decade following the impact (see Fig. 2, Fig. S3 and  
236 Fig. S4).

237 Over land, crocodylomorphs (a group including crocodilians), chelonians (the order  
238 containing turtles), and champsosaurs with representatives in shallow marine and freshwater  
239 habitats seem to have survived better than other large bodied fauna [Benton, 1993, MacLeod *et*  
240 *al.*, 1997, Martin *et al.*, 2014]. Large rivers might have been somewhat insulated from terrestrial  
241 temperature changes and fires, while estuarine areas might not have felt the full effects of marine  
242 stratification on nutrient supply: species living in such habitats might have therefore survived  
243 better than their fully oceanic or terrestrial counterparts, especially if they were tolerant to a wide  
244 range of different body temperatures.

245 The once in  $\sim 10^7$ - $10^8$  year occurrence of 10 km bolide impacts [Toon *et al* 1997] raises  
246 the possibility that such impacts could have played a role in the deglaciation of the  
247 Neoproterozoic snowball-Earth, given the  $\sim 5 \times 10^7$  yr timescale of the event. If the Earth’s tropics

248 had been covered with ice and snow to any degree, the absence of weathering would cause CO<sub>2</sub>  
249 to build up in the atmosphere. However, even such CO<sub>2</sub> forcing is thought to have been too weak  
250 to deglaciate the tropical oceans if taken alone [e.g. *Le Hir et al.*, 2010]. In this situation, a bolide  
251 impact over a shallow sea would not only potentially provide a positive radiative forcing through  
252 darkening the tropical cryosphere by solid ejecta in a similar manner that has been postulated for  
253 the effects of dust (Abbot And Pierrehumbert 2010), but would also provide intense, if short-  
254 lived, SWV and cloud radiative forcings that might trigger deglaciation by amplifying the effect  
255 of the high background levels of CO<sub>2</sub>. Future research should attempt to quantify both forcing  
256 and feedback effects further, given their sensitivity to the mean background state [*Pierrehumbert*  
257 *et al.* 2011].

258 Owing to the large uncertainties involved, we have not considered possible  
259 microphysical-chemical-climatic interactions following an impact event, such as: ozone  
260 depletion associated with large amounts of injected halogen-containing sea salt aerosol [*Pierazzo*  
261 *et al.*, 2010]; changes to SWV lifetime associated with increased oxidation of CH<sub>4</sub> by chlorine  
262 atoms; or HOx produced by large amounts of SWV. Large stratospheric aerosol loading might  
263 act to scavenge water, thus reducing SWV [*Pierazzo et al.*, 2010]. However, assuming a particle  
264 radius of 0.5 μm, a submicron aerosol source from the impact [*Toon et al.*, 1997] and an upper  
265 limit for a growth factor of sulphate aerosol of 5x (based on the growth of sulfuric acid particles  
266 under stratospheric conditions) we estimate that only a few percent of the SWV would be taken  
267 up by aerosol. Microphysical effects such as coagulation would also lower the magnitude of the  
268 RF from sulfate aerosol by increasing particle size [*Timmreck et al.*, 2010], as well as reducing  
269 aerosol residence time [*Pierazzo et al.*, 2003]. Additionally, a large stratospheric aerosol loading  
270 would warm the tropical tropopause, which might further increase SWV [*Joshi and Shine*, 2003].  
271 Ice crystals might form, but even in the case with 300 ppm of SWV the stratosphere would only  
272 be supersaturated with respect to ice below about 20 km in altitude. Furthermore, there is a large  
273 uncertainty in the radiative effect of ice crystals because of factors such as ice crystal size and  
274 cloud optical depth [*Emiliani et al.*, 1981], which in turn depend on a variety of different  
275 processes, so the effects of ice crystals have not been considered here. The exact composition of  
276 aerosol (e.g. soot, dust, sulphate) would be expected to be different for different impact events.  
277 CO<sub>2</sub> increases resulting from impact events are extremely uncertain [*Royer*, 2014, *Huang et al.*,  
278 2013], and have not been considered here.

279 We have explored potential climatic scenarios following extraterrestrial bolide impacts  
280 over the ocean that significantly raise stratospheric water vapor (SWV) levels. While short-term  
281 cooling and reduced primary productivity is likely to occur for impacts releasing aerosol into the  
282 atmosphere, the effects of increasing SWV may include rapid climate warming and increased  
283 ocean stratification on a timescale of 1-2 decades. The process could improve our understanding  
284 of periods such as the K-Pg extinction or the deglaciation of the Neoproterozoic snowball Earth,  
285 and indeed might reconcile differing viewpoints on the temporal and causal relationship between  
286 the Chicxulub impact and the K-Pg event itself [*Archibald et al.*, 2010, *Schulte et al.*, 2010].

287

288

289

## 290 Acknowledgments

291 We acknowledge the support of resources provided by UK National Centre for Atmospheric  
292 Science (NCAS), the High Performance Computing Cluster supported by the Research and  
293 Specialist Computing Support service at the University of East Anglia, UK Natural Environment  
294 Research Council (NERC), grants "CPE" (NE/K014757/1), and "Paleopolar" (NE/I005722/1). .  
295 Data can be obtained from MJ on request. ACM acknowledges support from an AXA  
296 Postdoctoral Fellowship and the ERC ACCI grant Project No 267760, and NERC grant  
297 NE/M018199/1. We gratefully acknowledge the contribution of Roland Von Glasow, who  
298 played an integral role in the preparation of the original manuscript, but sadly passed away  
299 before its submission to Geophysical Research Letters. We also acknowledge useful input from  
300 K. Shine and J. Laube.

301

## 302 References

- 303 Abbot, D. S., and R. T. Pierrehumbert (2010), Mudball: Surface dust and snowball Earth  
304 deglaciation, *J. Geophys. Res.*, 115, D03104, doi:10.1029/2009JD012007.
- 305 Alegret, L., E. Thomas, and K. C. Lohmann (2012), End-Cretaceous marine mass extinction not  
306 caused by productivity collapse, *Proc. Natl. Acad. Sci. U.S.A.*, 109, 728-732.
- 307 Alvarez, L. W., W. Alvarez, F. Asaro, and H. V. Michel (1980), Extraterrestrial Cause for the  
308 Cretaceous-Tertiary Extinction, *Science*, 208, 1095-1108.
- 309 Archibald, J. D. et al. (2010), Cretaceous Extinctions: Multiple Causes, *Science*, 328, 973.
- 310 Benton, M. J. (1993), In *The Fossil Record 2*, Benton, M. J. Ed. (Chapman and Hall), pp 681-  
311 737.
- 312 Collins, M. et al. (2013), Long-term Climate Change: Projections, Commitments and  
313 Irreversibility. In: *Climate Change 2013: The Physical Science Basis. Contribution of*  
314 *Working Group I to the Fifth Assessment Report of the Intergovernmental Panel on*  
315 *Climate Change [Stocker, T.F. et al. (eds.)]. Cambridge University Press, Cambridge,*  
316 *United Kingdom and New York, NY, USA.*
- 317 Covey, C., S. L. Thompson, P. R. Weissman, and M. C. MacCracken (1994), Global climatic  
318 effects of atmospheric dust from an asteroid or comet impact on Earth, *Global Planet.*  
319 *Change*, 9, 263-273.
- 320 Emiliani, C, E. B. Kraus, and E. M. Shoemaker (1981), Sudden death at the end of the Mesozoic,  
321 *Earth Planetary. Sci.*, 55, 317-334.
- 322 Engel, A. et al. (2009), Age of stratospheric air unchanged within uncertainties over the past 30  
323 years, *Nature Geosci.*, 2, 28-31.
- 324 Gordon, C. et al. (2000), The simulation of SST, sea ice extents and ocean heat transports in a  
325 version of the Hadley Centre coupled model without flux adjustments, *Clim. Dynam.*, 16,  
326 147-168.



- 327 Gregg, W. W., M. E. Conkright, P. Ginoux, J. E. O'Reilly, and N. W. Casey (2003) Ocean  
328 primary production and climate: Global decadal changes, *Geophys. Res. Lett.*, 30, 1809,  
329 doi: 10.1029/2003GL016889
- 330 Gregory, J. M. et al. (2004), A new method for diagnosing radiative forcing and climate  
331 sensitivity, *Geophys. Res. Lett.*, 31, L03205, doi:10.1029/2003GL018747.
- 332 Huang, C., G. J. Retallack, C. Wang, and Q. Huang (2013), Paleoatmospheric pCO<sub>2</sub> fluctuations  
333 across the Cretaceous–Tertiary boundary recorded from paleosol carbonates in NE China,  
334 *Palaeogeogr. Palaeoclimatol. Palaeoecol.*, 385, 95-105.
- 335 Hunter, S. J., A. M. Haywood, P. J. Valdes, J. E. Francis, and M. J. Pound (2013), Modelling  
336 equable climates of the Late Cretaceous: Can new boundary conditions resolve data–  
337 model discrepancies? *Palaeogeogr. Palaeoclimatol. Palaeoecol.*, 392, 41–51.
- 338 Kaiho, K., N. Oshima, K. Adachi, Y. Adachi, T. Mizukami, M. Fujibayashi, R. Saito (2016),  
339 Global climate change driven by soot at the K-Pg boundary as the cause of the mass  
340 extinction, *Sci. Rep.*, 6, 28427, DOI: 10.1038/srep28427.
- 341 Le Hir., G., Y. Donnadieu, G. Krinner, and G. Ramstein (2010), Toward the snowball earth  
342 deglaciation..., *Clim. Dynam.*, 35, 285-297.
- 343 Lunt, D. J. et al. (2016), Palaeogeographic controls on climate and proxy interpretation, *Clim.*  
344 *Past*, 12, 1181-1198, doi:10.5194/cp-12-1181-2016.
- 345 MacLeod, N. et al. (1997), The Cretaceous–Tertiary biotic transition, *J. Geol. Soc.*, 154, 265–  
346 292.
- 347 Markwick, P. J., and P. J. Valdes (2004), Palaeo-digital elevation models for use as boundary  
348 conditions in coupled ocean-atmosphere GCM experiments: a Maastrichtian (late  
349 Cretaceous), example, *Palaeogeogr., Palaeoclimatol., Palaeoecol.*, 213, 37-63.
- 350 Martin, J. E., R. Amiot, C. Lécuyer, and M. J. Benton (2014), Sea surface temperature  
351 contributes to marine crocodylomorph evolution, *Nat. Commun.*, 5, 4658.
- 352 Maycock, A., K. Shine, and M. Joshi (2011), The temperature response to stratospheric water  
353 vapour changes, *Quart. J. Royal Meteorol. Soc.*, 137, 1070-1082.
- 354 Maycock, A. C., M. M. Joshi, K. P. Shine, and A. A. Scaife (2013), The Circulation Response to  
355 Idealized Changes in Stratospheric Water Vapor, *J. Climate*, 26, 545-561.
- 356 Oerder, V., Colas, F., Echevin, V., Codron, F., Tam, J., and Belmadani, A. (2015), Peru-Chile  
357 upwelling dynamics under climate change, *J. Geophys. Res.*, 120, 1152-1172.
- 358 Pierazzo, E., A. N. Hahmann, and L. C. Sloan (2003), Chicxulub and Climate: Radiative  
359 Perturbations of Impact-Produced S-Bearing Gases, *Astrobiology*, 1, 99-118.
- 360 Pierazzo, E., et al. (2010), Ozone perturbation from medium-size asteroid impacts in the ocean,  
361 *Earth Planetary. Sci.*, 299, 263-272.
- 362 Pierrehumbert, R. T., D. S. Abbot, A. Voigt, and D. Koll (2011), Climate of the Neoproterozoic,  
363 *Ann. Rev. Earth. Planetary Sci.*, 39, 417-460.
- 364 Roemmich, D., and McGowan, J (1995) Climatic Warming and the Decline of Zooplankton in  
365 the California Current, *Science*, 267, 1324-1326.

366 Royer, D. L. (2014), Atmospheric CO<sub>2</sub> and O<sub>2</sub> during the Phanerozoic: tools, patterns, and  
367 impacts in *Treatise on Geochemistry* (2nd Edition), (Elsevier), chap. 6, pp. 251–267.

368 Schulte, P. et al. (2010), The Chicxulub Asteroid Impact and Mass Extinction at the Cretaceous-  
369 Paleogene Boundary, *Science*, 327, 1214-1218.

370 Shine, K. P., J. S. Fuglestedt, K. Hailemariam, and N. Stuber (2005), Alternatives to the Global  
371 Warming Potential for Comparing Climate Impacts of Emissions of Greenhouse Gases,  
372 *Climatic Change*, 68, 281-302.

373 Smith, R. S. (2012a), The FAMOUS climate model (versions XFXWB and XFHCC): description  
374 update to version XDBUA, *Geosci. Model Dev.*, 5, 269–276.

375 Smith, R., S. and Gregory, J. M. (2012b), The last glacial cycle: transient simulations with an  
376 AOGCM, *Climate Dynamics*, 38, 1545-1559.

377 Timmreck, C. et al. (2010), Aerosol size confines climate response to volcanic super-eruptions,  
378 *Geophys. Res. Lett.*, 37, L24705, doi:10.1029/2010GL045464.

379 Toon, O. B., K. Zahnle, D. Morrison, and R. P. Turco, and C. Covey (1997), Environmental  
380 perturbations caused by the impact of asteroids and comets, *Rev. Geophys.* 35, 41-78.

381

382

### 383 Figure Captions

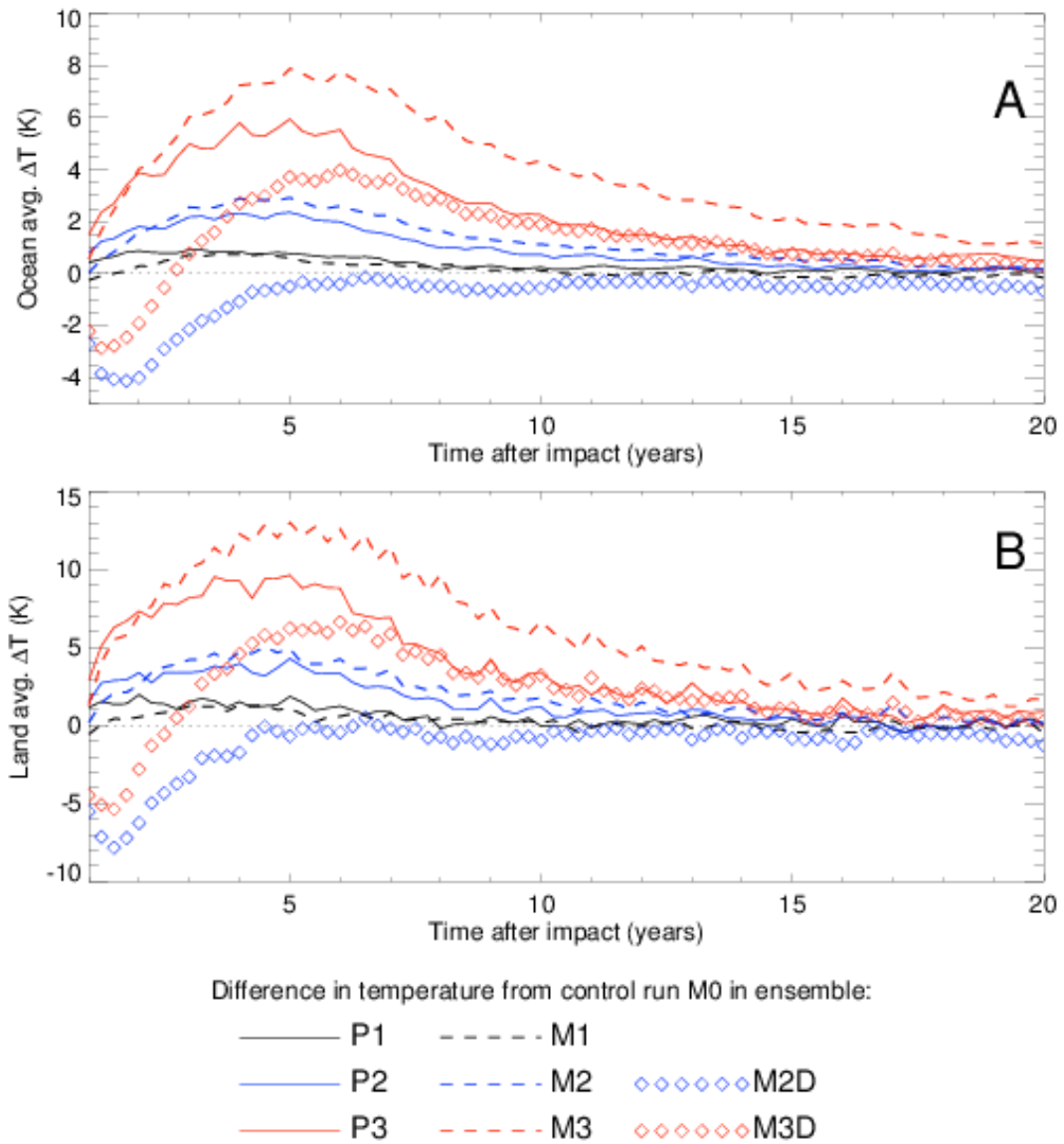
384 **Figure 1. (a)**, Evolution of area-averaged surface air temperatures over the ocean (K), with time  
385 after the impact event. The lines show differences between P1-P0 (black solid); M1-M0 (black  
386 dashed); P2-P0 (blue solid); M2-M0 (blue dashed); P3-P0 (red solid); M3-M0 (red dashed);  
387 M2D-M0 (blue diamonds); M3D-M0 (red diamonds). **(b)**, as (a), but for the difference in area-  
388 averaged surface air temperature over land (K). The thin dotted lines clarify 0 K changes.

389 **Figure 2. (a)**, Latitude-depth cross section of the difference in zonally-averaged potential  
390 temperature (K), in the top 300m of the ocean between ensembles P2 (averaged in time between  
391 years 1 and 10 after the impact) and P0. Regions having values smaller than one interannual  
392 standard deviation in the control run are hatched in order to demonstrate the size of the signal  
393 compared to simulated natural variability. **(b)**, as (a), but for difference between ensembles P3  
394 and P0. **(c)**, as (a), but for difference between ensembles M3 and M0. **(d)**, as (a), but for  
395 difference between ensembles M3D and M0. Note the nonlinear contour intervals in each panel.

396 **Figure 3. (a)**, Minimum annually averaged temperature change over land (K), between years 0-  
397 10 after a simulated impact calculated using several hundred simulations of the EBM showing  
398 the combined effect of aerosol and SWV RF<sup>8</sup>. The abscissa shows the most negative aerosol RF  
399 ( $\text{Wm}^{-2}$ ), and the ordinate shows the maximum value of SWV RF ( $\text{Wm}^{-2}$ ), in each individual  
400 EBM run. **(b)**, as (a), but for the maximum annually averaged ocean mixed layer temperature  
401 response (K). FAMOUS ensembles M2, M2D, M3 and M3D are marked in grey in positions  
402 corresponding to their initial radiative forcings for comparison.

### 403 Table Captions

404 **Table 1.** Description of ensembles, maximum SWV perturbation, RF using radiative model of  
405 *Maycock et al*, [2011], regressed RF in Preindustrial (P), Maastrichtian (M), and Maastrichtian +  
406 Dimming (MD), cases, approximate corresponding impactor diameter, energy and return period  
407 [*Toon et al.*, 1997, *Emiliani et al.*, 1981].  
408

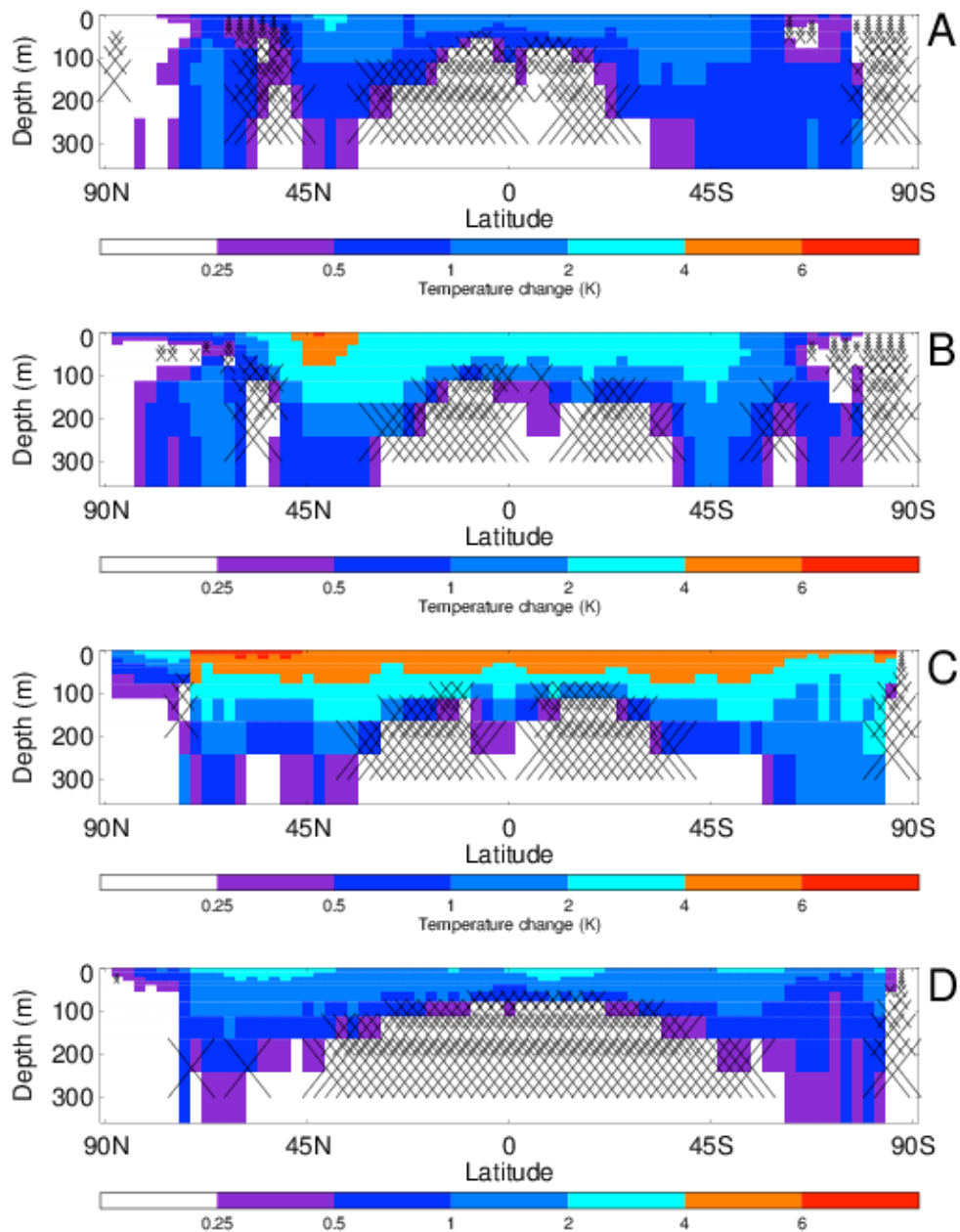


409

410 **Figure 1. (a)**, Evolution of area-averaged surface air temperatures over the ocean (K), with time  
 411 after the impact event. The lines show differences between P1-P0 (black solid); M1-M0 (black  
 412 dashed); P2-P0 (blue solid); M2-M0 (blue dashed); P3-P0 (red solid); M3-M0 (red dashed);  
 413 M2D-M0 (blue diamonds); M3D-M0 (red diamonds). **(b)**, as (a), but for the difference in area-  
 414 averaged surface air temperature over land (K). The thin dotted lines clarify 0 K changes.

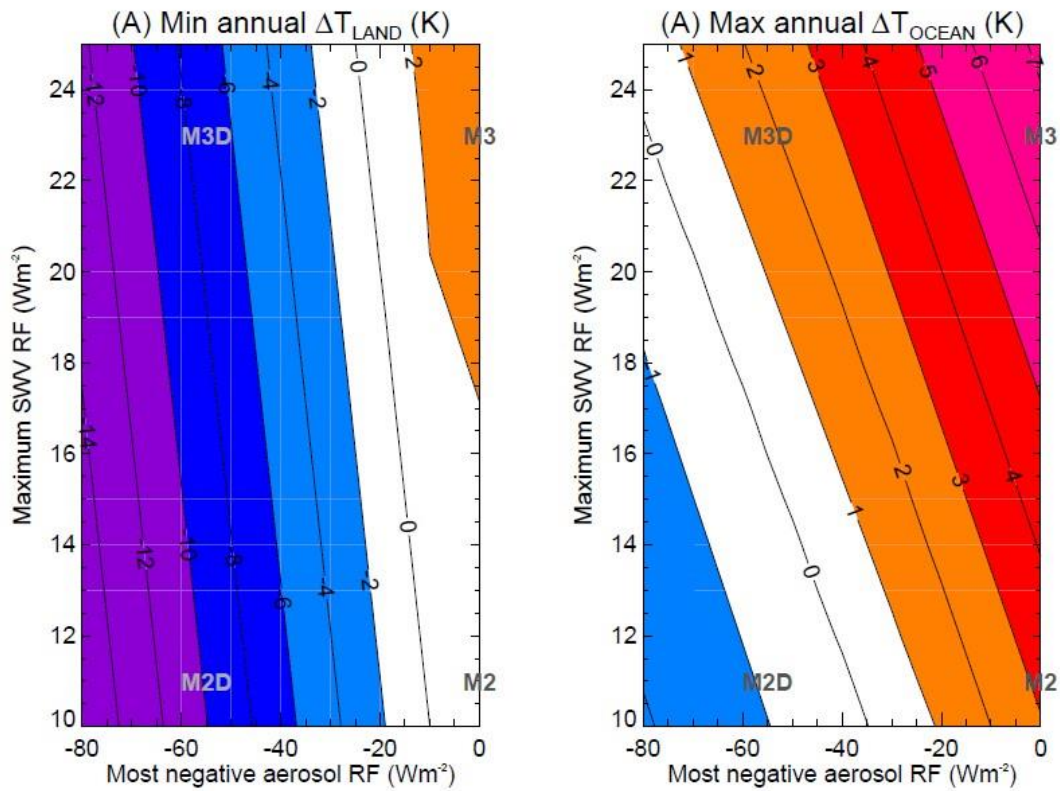
415

416



417

418 **Figure 2. (a)**, Latitude-depth cross section of the difference in zonally-averaged potential  
 419 temperature (K), in the top 300m of the ocean between ensembles P2 (averaged in time between  
 420 years 1 and 10 after the impact) and P0. Regions having values smaller than one interannual  
 421 standard deviation in the control run are hatched in order to demonstrate the size of the signal  
 422 compared to simulated natural variability. **(b)**, as (a), but for difference between ensembles P3  
 423 and P0. **(c)**, as (a), but for difference between ensembles M3 and M0. **(d)**, as (a), but for  
 424 difference between ensembles M3D and M0. Note the nonlinear contour intervals in each panel.  
 425



426

427 **Figure 3. (a)**, Minimum annually averaged temperature change over land (K), between years 0-  
 428 10 after a simulated impact calculated using several hundred simulations of the EBM showing  
 429 the combined effect of aerosol and SWV RF<sup>8</sup>. The abscissa shows the most negative aerosol RF  
 430 ( $\text{Wm}^{-2}$ ), and the ordinate shows the maximum value of SWV RF ( $\text{Wm}^{-2}$ ), in each individual  
 431 EBM run. **(b)**, as (a), but for the maximum annually averaged ocean mixed layer temperature  
 432 response (K). FAMOUS ensembles M2, M2D, M3 and M3D are marked in grey in positions  
 433 corresponding to their initial radiative forcings for comparison.

434

435

436

437

438

439

440

441

442

443

444

445

446

447

448

449

450

451

452

453

454

455

456

Impactor diameter (km)	-	~1	~3	~10
Impactor Energy (Mt)	-	$10^4$ - $10^5$	$\sim 10^6$	$10^7$ - $10^8$
Impactor return period (years)	-	$\sim 10^5$	$\sim 10^6$	$\sim 10^7$ - $10^8$
SWV <sub>max</sub> perturbation (ppm)	0	10	50	300
RF calculated using radiative model ( $\text{Wm}^{-2}$ )	-	3.8	9.2	19.2
Preindustrial Runs	<b>P0</b>	<b>P1</b>	<b>P2</b>	<b>P3</b>
Maximum regressed preindustrial SWV RF ( $\text{Wm}^{-2}$ )	-	$3.4 \pm 1.5$	$10.6 \pm 2.0$	$22.0 \pm 1.6$
Maastrichtian Runs	<b>M0</b>	<b>M1</b>	<b>M2</b>	<b>M3</b>
Maximum regressed Maastrichtian SWV RF ( $\text{Wm}^{-2}$ )	-	$1.8 \pm 1.4$	$11.1 \pm 1.2$	$22.9 \pm 0.8$
Maastrichtian Runs with dimming	<b>M0</b>	-	<b>M2D</b>	<b>M3D</b>
Minimum value of surface solar dimming ( $\text{Wm}^{-2}$ )			-55	-55

457 **Table 1.** Description of ensembles, maximum SWV perturbation, RF using radiative model of  
 458 *Maycock et al.*, [2011], regressed RF in Preindustrial (P), Maastrichtian (M), and Maastrichtian +  
 459 Dimming (MD), cases, approximate corresponding impactor diameter, energy and return period  
 460 [*Toon et al.*, 1997, *Emiliani et al.*, 1981].

461

462

463

464

465  
466  
467  
**468**  
469  
470  
471  
472  
473  
474  
475  
476  
477  
478  
479  
480  
481  
**482**  
483  
484  
485  
486  
487  
488  
489  
490

*Geophysical research Letters*

Supporting Information for

**Global warming and ocean stratification: a potential result of large extraterrestrial impacts**

Manoj Joshi<sup>1,2</sup>, Roland von Glasow<sup>1</sup>, Robin Smith<sup>3</sup>, Charles G. M. Paxton<sup>4</sup>, Amanda C. Maycock<sup>5,6</sup>, Daniel Lunt<sup>7</sup>, Claire Loptson<sup>7</sup>, Paul Markwick<sup>8</sup>

<sup>1</sup> Climatic Research Unit, School of Environmental Sciences, University of East Anglia, Norwich, U.K.

<sup>2</sup> Centre for Ocean and Atmospheric Sciences, School of Environmental Sciences, University of East Anglia, Norwich, U.K.

<sup>3</sup> National Centre for Atmospheric Science, University of Reading, U.K.

<sup>4</sup> Centre for Research into Ecological and Environmental Modelling, University of St Andrews, St Andrews, U.K.

<sup>5</sup> Centre for Atmospheric Science, Department of Chemistry, University of Cambridge, Cambridge, U.K.

<sup>6</sup> National Centre for Atmospheric Science, University of Cambridge, U.K.

<sup>7</sup> School of Geographical Sciences, University of Bristol, Bristol, U.K.

<sup>8</sup> Getech PLC, Leeds, U.K.

**Contents of this file**

Text S1 to S2  
Figures S1 to S4



## 491 Introduction

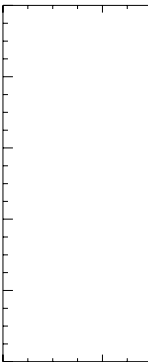
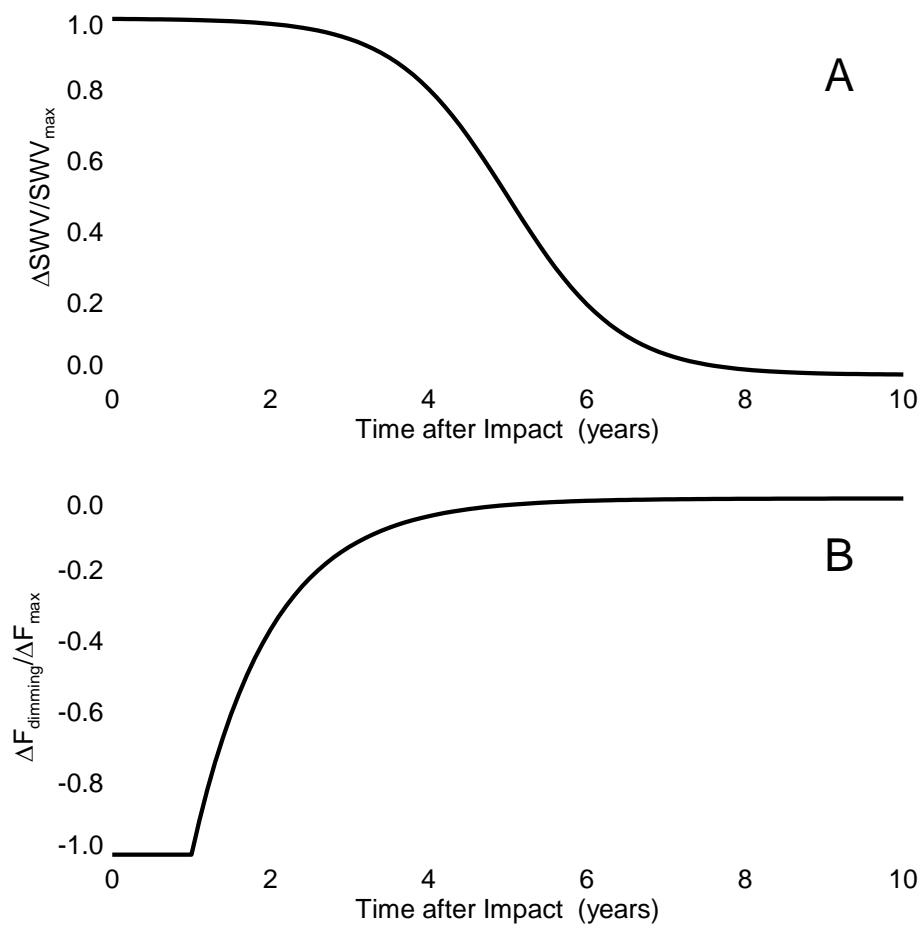
492 The supporting information consists of details of the two numerical models used, and four figures.

493 **Text S1.** Here we use version XFHCC of FAMOUS [Smith *et al.*, 2012], which applies a simple Rayleigh  
494 friction term over the top 3 levels of the atmosphere to parameterize the effects of breaking gravity or  
495 buoyancy waves that are poorly represented at this horizontal resolution. This significantly improves  
496 both the representation of the upper troposphere/lower stratosphere in FAMOUS and measures of  
497 troposphere variability. A simple parameterization specifies stratospheric ozone levels interactively  
498 based on whether they are below, at or above the tropopause, taking values derived from a modern  
499 climatology. The “pre-industrial” (denoted P) configuration (see Table 1) has greenhouse gases such as  
500 CO<sub>2</sub> and other boundary conditions such as continental distribution set to their values in 1850. The  
501 Maastrichtian configuration (denoted M) uses paleogeography (topography and bathymetry) created  
502 using similar techniques to previous work [Hunter *et al.*, 2013], based on published lithologic, tectonic  
503 and fossil studies, the lithologic databases of the Paleogeographic Atlas Project (University of Chicago),  
504 and deep sea (DSDP/ODP) data, underpinned by a globally integrated plate model based on structural  
505 geology, plate kinematics and geophysics [Markwick and Valdes, 2013]. The Maastrichtian runs use  
506 preindustrial levels of CO<sub>2</sub>, which is on the lowest end of estimates of CO<sub>2</sub> during the end of the  
507 Cretaceous period [Royer, 2014], but still produce realistic amount of climatological Maastrichtian  
508 warming compared to the present day.

509 The pre-industrial control simulation for this version of FAMOUS was spun up for a thousand years,  
510 initialised from the pre-industrial climate of version XFXWB [Smith *et al.*, 2012] which had been run for  
511 more than 5000 years. The Maastrichtian spinup simulation was partly initialised from a HadCM3L  
512 simulation of the Maastrichtian time period which used the TRIFFID dynamic vegetation model [Lunt *et al.*,  
513 2015]. The ocean state was used directly from the same HadCM3L simulation, which had been  
514 initialized as stationary with no initial flow, with an idealized zonally averaged temperature structure  
515 and salinity set to a constant 35 ppt, and run for 14,00 years. Spatially-varying land surface properties  
516 (e.g. vegetation fraction and albedo) were derived from the HadCM3L simulation. The atmosphere was  
517 initialized from an arbitrary atmospheric state from a previous preindustrial simulation. FAMOUS was  
518 then spun up for 5000 years.

519 The RFs for the perturbed ensembles are shown in Table 1, and are calculated by plotting the simulated  
520 net flux at the top of the atmosphere against the globally averaged surface temperature difference  
521 between years 0-4 after the simulated impact and 10 different 4-year long segments of the relevant  
522 control run. The 4-year period is chosen as a balance between overestimation of RF from using too long  
523 a timescale when the RF is decreasing with time (see Figure 1), and very large uncertainties produced  
524 from using a shorter timescale. The plots are regressed to year 0 (i.e.: the time of impact), in a similar  
525 manner to previous methods [Gregory *et al.*, 2004], with the 95% confidence interval shown (see Table  
526 1). The RF values in FAMOUS can be compared with results from a more complex radiative code with 15  
527 levels in the stratosphere up to the 0.8 hPa level, which allows stratospheric temperatures to respond to  
528 the SWV perturbation, but does not allow any tropospheric change [Maycock *et al.*, 2011]. The RF  
529 values produced with the more complex code are approximately 10% smaller than the values produced  
530 by FAMOUS, showing that the SWV RF in FAMOUS is reasonable despite having only 2-3 levels in the  
531 stratosphere. The climate feedback parameter in FAMOUS is  $1.10 \pm 0.05 \text{ Wm}^{-2} \text{ K}^{-1}$ , which is similar to  
532 HadCM3, being  $1.32 \pm 0.08 \text{ Wm}^{-2} \text{ K}^{-1}$ , showing that the climate response of FAMOUS is consistent with  
533 other models used in global assessments of contemporary climate change [Collins *et al.*, 2013].

534



535

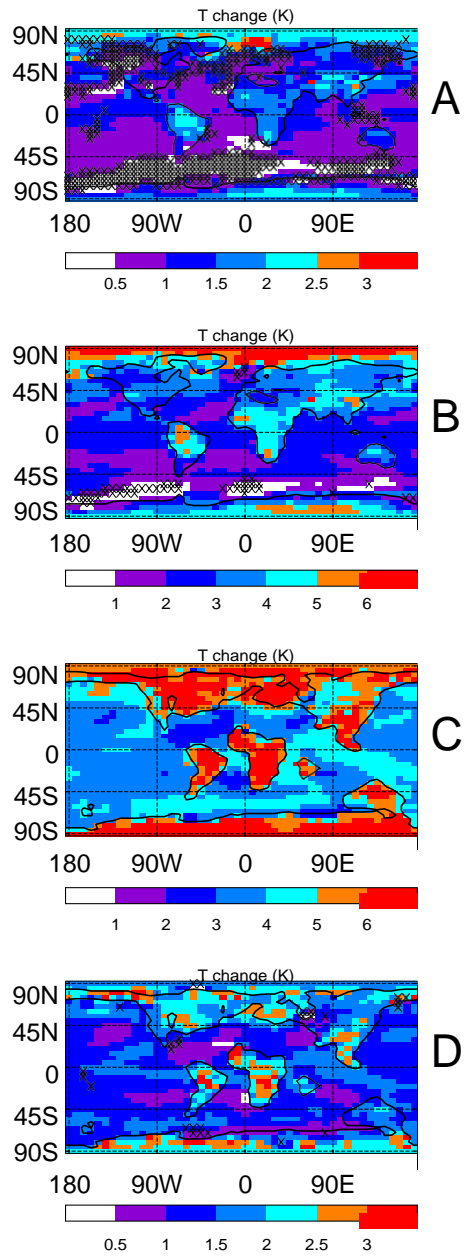
536

537

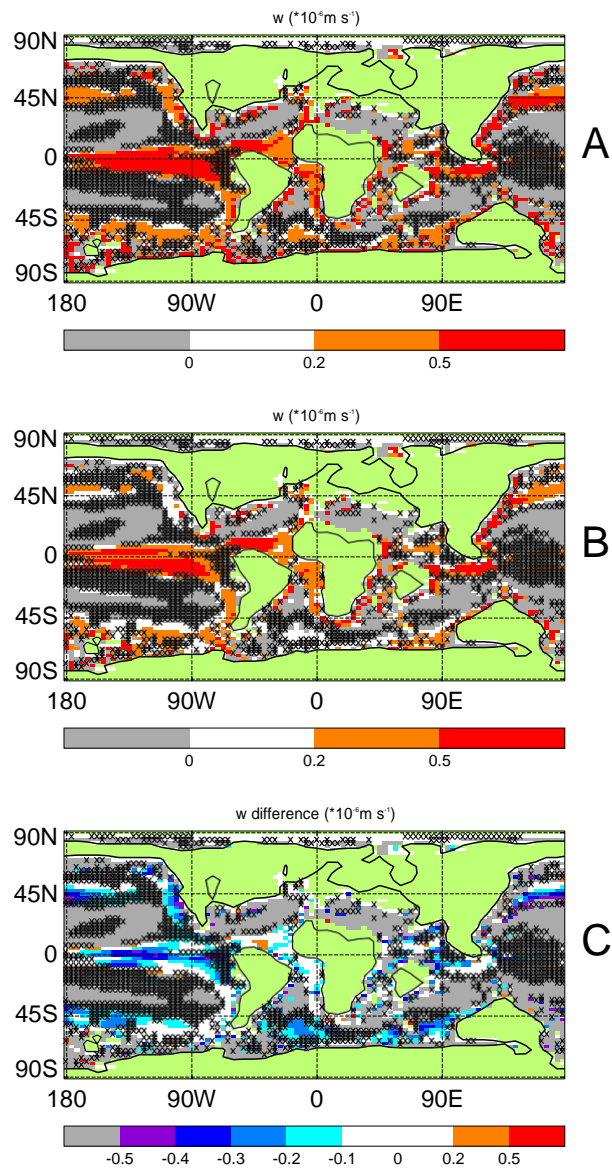
538

**Figure**

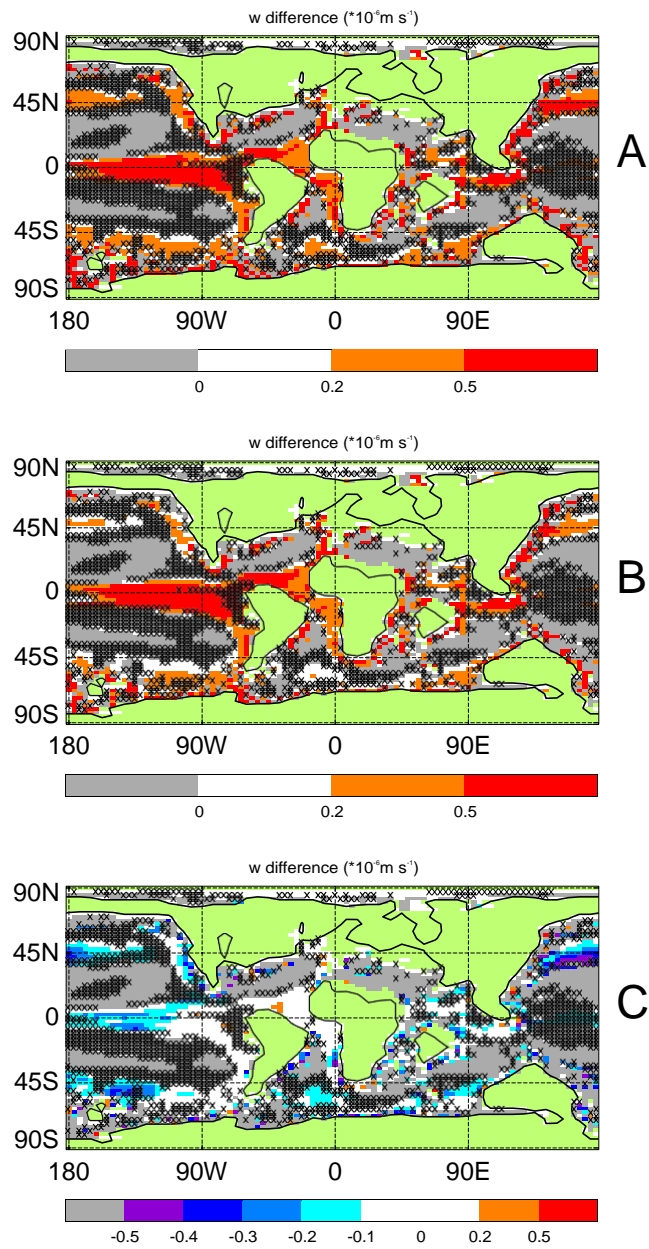
**S1.** (a) Evolution of imposed SWV RF in FAMOUS normalized by  $SWV_{max}$ , whose values are given in Table 1 for each model ensemble. (b) Evolution of imposed solar dimming RF in FAMOUS normalized by its maximum amplitude, whose values are given in Table 1 for each model ensemble.



539  
 540 **Figure S2.** (a) Difference in surface air temperature (K) between ensembles P2 and Po averaged in time  
 541 between years 1.0 to 10.0 after the impact. Regions having values smaller than one interannual  
 542 standard deviation in the control run Po are hatched. (b) as (a) but for difference between P3 and Po. (c)  
 543 as (a) but for difference between M3 and Mo. (d) as (a) but for difference between M3D and Mo.  
 544



545  
 546 **Figure S3.** (a) Map of vertical velocity ( $10^{-6} \text{ m s}^{-1}$ , upwards positive) at 96 m below the surface, i.e. below  
 547 the mixed layer in the tropics and subtropics in run Mo. Areas with downwelling i.e. negative velocities  
 548 have been greyed out for clarity. Regions having values smaller than one interannual standard deviation  
 549 in the control run are hatched. (b) as (a) but for ensemble M3 in years 1-10 following the simulated  
 550 impact. (c) Map of (b) minus (a); greyed out areas are as in (a), i.e. downwelling regions. In most  
 551 upwelling zones vertical velocities have been reduced by up to 50%, which restricts nutrient supply to  
 552 the topmost 100 m of the ocean.



553

554 **Figure S4.** (a) as Fig. 3. (b), (c) as Fig. 3 but for ensemble M<sub>3</sub>D.

555

556